


Article

In-Plane Anisotropic Thermal Conductivity of Low-Symmetry PdSe₂

Lijie Chen ¹, Weitao Zhang ¹ , Hanlin Zhang ¹, Jiawang Chen ¹, Chaoyang Tan ¹, Shiqi Yin ¹, Gang Li ¹, Yu Zhang ¹, Penglai Gong ² and Liang Li ^{1,3,*}

- ¹ Information Materials and Intelligent Sensing Laboratory of Anhui Province, Institutes of Physical Science and Information Technology, Anhui University, Hefei 230601, China; chenlj96@163.com (L.C.); q18201126@stu.ahu.edu.cn (W.Z.); q19301148@stu.ahu.edu.cn (H.Z.); chenjlw@mail.ustc.edu.cn (J.C.); tancy1125@163.com (C.T.); q19201097@stu.ahu.edu.cn (S.Y.); q19101003@stu.edu.cn (G.L.); dayu@ahu.edu.cn (Y.Z.)
- ² Department of Physics, Southern University of Science and Technology, Shenzhen 518055, China; gongpl@sustc.edu.cn
- ³ Key Laboratory of Structure and Functional Regulation of Hybrid Materials (Anhui University), Ministry of Education, Institutes of Physical Science and Information Technology, Anhui University, Hefei 230601, China
- * Correspondence: liangli@ahu.edu.cn

Abstract: Low-symmetry two-dimensional (2D) materials have exhibited novel anisotropic properties in optics, electronics, and mechanics. Such characteristics have opened up new avenues for fundamental research on nano-electronic devices. In-plane thermal conductivity plays a pivotal role in the electronic performance of devices. This article reports a systematic study of the in-plane anisotropic thermal conductivity of PdSe₂ with a pentagonal, low-symmetry structure. An in-plane anisotropic ratio up to 1.42 was observed by the micro-Raman thermometry method. In the Raman scattering spectrum, we extracted a frequency shift from the A_g³ mode with the most sensitivity to temperature. The anisotropic thermal conductivity was deduced by analyzing the heat diffusion equations of suspended PdSe₂ films. With the increase in thickness, the anisotropy ratio decreased gradually because the thermal conductivity in the *x*-direction increased faster than in the *y*-direction. The anisotropic thermal conductivity provides thermal management strategies for the next generation of nano-electronic devices based on PdSe₂.

Keywords: PdSe₂; thermal conductivity; Raman spectrum



Citation: Chen, L.; Zhang, W.; Zhang, H.; Chen, J.; Tan, C.; Yin, S.; Li, G.; Zhang, Y.; Gong, P.; Li, L. In-Plane Anisotropic Thermal Conductivity of Low-Symmetry PdSe₂. *Sustainability* **2021**, *13*, 4155. <https://doi.org/10.3390/su13084155>

Academic Editor:
Konstantinos Dimos

Received: 18 March 2021
Accepted: 6 April 2021
Published: 8 April 2021

Publisher's Note: MDPI stays neutral with regard to jurisdictional claims in published maps and institutional affiliations.



Copyright: © 2021 by the authors. Licensee MDPI, Basel, Switzerland. This article is an open access article distributed under the terms and conditions of the Creative Commons Attribution (CC BY) license (<https://creativecommons.org/licenses/by/4.0/>).

1. Introduction

Two-dimensional (2D) materials have rapidly attracted widespread attention as promising materials for their novel physical properties and dramatic application prospects [1–4]. After discovering and studying 2D materials such as graphene and black phosphorus (BP), scientific and engineering communities are more inclined to seek materials with adjustable band gaps and relative environmental stability. Recently, a new family of 2D materials, noble-metal dichalcogenides (NMDCs: MX₂, M = Pd, Pt, X = S, Se), has inspired interest because of their strong interlayer interactions and remarkable layer-dependent physical properties [5–9]. Besides, NMDCs have shown outstanding performance in electron and photoelectric devices with high air stability, such as a field-effect transistor (FET) with a tunable ambipolar charge carrier [10] and a photoelectric detector with high sensitivity [11]. Among them, PdSe₂ possesses an infrequently puckered low-symmetry pentagonal, layered structure. This unique atomic arrangement leads to interesting mechanical properties, including unusual negative Poisson's ratio and ultra-high mechanical strength [12–15]. Notably, this low-symmetry structure offers new characteristics for in-plane anisotropy in optics and electronics [16,17]. For example, PdSe₂ possesses a strong linear dichroism ratio, up to 1.9, which can act as a high polarization-sensitive

photodetector [18,19]. Notably, both chemical vapor deposition (CVD) grown and exfoliated PdSe₂ exhibit extremely high air quality stability and device performance stability, which provides an excellent opportunity for future large-scale electronic device applications [20,21]. Interestingly, it has been forecasted that, in the in-plane directions, the carrier mobility along the x -direction would be greater than along the y -direction, yet thermal conductivity was the opposite [22]. This unique property indicates that PdSe₂ has significant potential for thermoelectric applications, probably providing greater freedom in the thermal nano-devices' design [21–25]. Although it has been theoretically predicted that the anisotropy ratio of in-plane thermal conductivity will reach 1.9 [22], experimental evidence is still lacking.

Hitherto, the micro-Raman thermometry (MRT) has been a common and effective method for the experimental study of thermal conductivity, which can directly and non-destructively explore the phonon information of semiconductor heat transfer. One of the significant advantages of the presented method is needless micro-nano device fabrication [26–28]. In this procedure, the laser focuses on the suspended film center to form a temperature gradient. With the increase in Raman laser power, the thermal conductivity can be extracted from the Raman spectrum's significant redshift due to phonon softening. Because of the anisotropic scattering of phonons in low-symmetric materials, MRT has been widely used in the study of anisotropic thermal conductivity, such as WTe₂, BP, and Te [26,29,30]. In this study, we systematically investigated the in-plane thermal conductivity of suspended PdSe₂ flakes with different thicknesses. Firstly, the lattice orientation was determined by angle-dependent polarized Raman spectra (ADPRS) and polarized-dependent optical absorption spectra. Then, the MRT method was used to measure the in-plane anisotropic thermal conductivity. The obtained anisotropic ratio of thermal conductivity was up to 1.42. The layer-dependent anisotropic thermal conductivity of PdSe₂ was also the first demonstration of 2D NMDCs, which is of great significance for the thermal management of the next generation of PdSe₂-based electronic devices.

2. Materials and Methods

A single crystal of PdSe₂ was purchased from HQ Graphene Company (purity = 99.998%). Few-layered PdSe₂ were mechanically exfoliated from bulk crystals at room temperature. The thinner flakes were initially identified by optical microscopy (WMJ-9688), utilizing polydimethylsiloxane (PDMS) transferred onto pre-cleaned, 200 nm Si₃N₄/Si with a hole of 6 μ m in diameter. The atomic force microscopy (AFM) images were obtained through the non-contact mode (Hitachi, AFM5500M).

Raman spectra were obtained by the FST2-Ahdx-DZ system using an incident laser (532 nm) in the back-scattering geometry. The detector was an Andor CCD with thermoelectric cooling to -60 °C. A 50 \times objective (numerical aperture = 0.42) was used to focus the incident light (e_i) and collect the Raman scattering (e_s) signal. In the parallel configuration ($e_i \parallel e_s$) and the cross configuration ($e_i \perp e_s$), the polarization direction (e_i) of the incident light was rotated every 15 degrees relative to the sample to obtain ADPRS. The temperature control was achieved by a Linkam thermal stage THMS600. The nitrogen atmosphere was maintained during the experiment to avoid the hydrolysis or oxidation of the PdSe₂ nanosheet.

3. Results and Discussion

The bulk PdSe₂ crystallizes in the space group of PbCa (point group D_{2h}) with an orthorhombic structure and unit cell of $a = 5.75$ Å and $b = 5.87$ Å [31,32]. The pentagonal lattice structure of PdSe₂ is shown in Figure 1a. The side view explicitly stresses the layered essence and the relationship of the van der Waals (vdW) forces in each layer. Pd and Se atoms show different configurations along the x - and y -directions, respectively. Typical layered structures had a single thickness of 6 Å [7], and each layer was coupled with a powerful van der Waals force (190 meV/atom) [21]. From the top view, we can see that the single layer of PdSe₂ was wholly composed of a pentagon ring, exhibiting a

unique pattern known as the Cairo pentagonal tiling. The pentagon has an asymmetric lattice structure and potential anisotropic physical properties exist in the plane [7,33,34]. Compared with other pentagonal 2D materials that are still in theory, PdSe₂ has already shown superior performance in practical applications [35–37]. A typical, non-polarized Raman spectrum of exfoliated PdSe₂ flakes on 200 nm Si₃N₄/Si substrate is shown in Figure S1 in the supplementary materials. Six prominent Raman peaks can be clearly observed. The 227 cm^{−1} peak can be attributed to the B_g modes, whereas the 144, 208, and 258 cm^{−1} peaks correspond to the A_g modes. Such a result is consistent with previous reports [38].

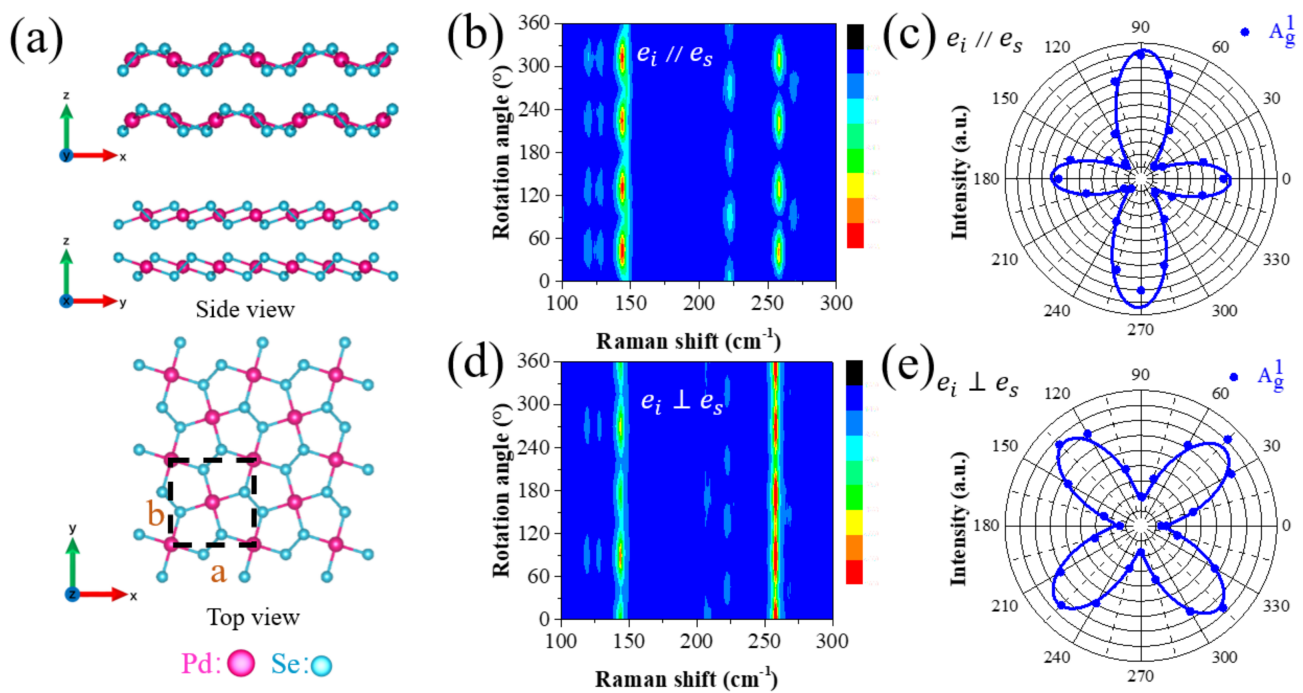


Figure 1. (a) Typical side view (up) and top view (down) of the layered, PdSe₂ anisotropic crystal structure. The contour maps of the angle-dependent polarized Raman spectra (ADPRS) of a PdSe₂ flake under (b) parallel-polarized and (d) cross-polarized configurations. Polar plots and fit curves of A_g¹ peak intensities under (c) parallel-polarized and (e) cross-polarized configurations.

In order to determine lattice orientation in thermal conductivity measurements, the ADPRS was employed to understand the anisotropic phonon vibration of PdSe₂. The contour map of parallel configuration is shown in Figure 1b, from which we can see that each of those peaks is shifting periodically (209 and 144 cm^{−1}), whereas others display a four-leaf pattern (e.g., 227 and 258 cm^{−1}). To demonstrate this phenomenon more clearly, we extracted the angle-dependent Raman intensity of a typical A_g¹ mode, as shown in Figure 1c, in which the maximum intensities occurred at 90° and 270°, and the secondary maxima at 0° and 180°. In contrast to the parallel configuration, the cross configuration presented another symmetric pattern, shown in Figure 1d. Most of them exhibited a four-leaf pattern (e.g., 118, 127, 144, and 258 cm^{−1}), and another displayed a two-leaf pattern (e.g., 208 cm^{−1}). Unlike parallel configurations, the polar plots of the angle-dependent Raman intensity of A_g¹ modes in cross configurations are shown in Figure 1e, which displays four-leaf patterns where the symmetry axis of the pattern was deflected by 45°, and the maximum intensities of all the A_g¹ modes were at 45°, 135°, 225°, and 295°. The ADPRS experimental findings were in full agreement with the relationship between the Raman tensor fitting (more details can be found in the Supplementary Material Note S1) and the angle of polarization orientation. The results indicate that the two in-plane principal

axes of PdSe₂ can be classified by ADPRS. However, since the Raman intensity was also related to the absorption of PdSe₂, the definitive *a* or *b* cannot be identified. Thus, after distinguishing the two in-plane principal axes, we employed polarized-dependent optical absorption spectra to confirm the in-plane lattice orientation [18].

Based on the unique linear dichroism transition of PdSe₂, for example, Figure S2 has shown the absorption intensity at 405 and 580 nm wavelengths, which have prominent angular dependence characteristics. It is easy to define the *x* and *y* lattice directions. For example, at 405 nm, the angle of the strongest absorption intensity corresponds to the *y*-direction, whereas, at 580 nm, the position of the strongest absorption intensity corresponds to the *x*-direction. Combining the optical absorption spectrum and Raman spectrum, we can determine the *x*-direction corresponding to the angle with a relatively large Raman intensity in *y* *A*_g¹ mode. These observations truly imply that the polarized Raman signals of PdSe₂ are intensely dependent on its crystalline orientation. This basic non-destructive process of ensuring crystal orientation is often commonly utilized in other 2D anisotropy materials [39,40].

To find the anisotropic thermal conductivity, we employed an MRT method to systematically study the thermal conductivity of 2D PdSe₂ [26,29,30]. Figure 2a shows the schematic diagram of the experimental setup, in which the polarized light was focused on the center of the hole, while the polarization direction of incident light was controlled by a rotating half-wave plate. The heat input and diffusion by the laser beam was subject to Gaussian distribution. Most heat was concentrated at the center of the suspended PdSe₂. The results provide a convenient way to obtain the temperature-related phonon information. To achieve high precision, the hole under the sample was much larger than the laser spot, which can minimize the substratum's influence and establish an appropriate temperature gradient from the hole center and the substrate. In our experiment, the hole diameter was 6 μm, which is adequate and much greater than the laser spot (about 2 μm); a typical suspended PdSe₂ is shown in the inset of Figure 2b. Then, we employed a temperature-dependent Raman spectrum under parallel configuration to obtain the temperature meter, reflecting Raman spectra's sensitivity to temperature. Embodying the temperature sensitivity of phonon vibration in PdSe₂, the two most apparent Raman peaks of 7.2 nm PdSe₂ are highlighted in Figure 2c. With the temperature increase from 100 K to room temperature, both the *A*_g¹ (145 cm^{−1}) and *A*_g³ (256 cm^{−1}) modes' peaks had a dramatic redshift, which originated from thermal expansion and anharmonic lattice vibrations [41,42]. Similarly, with the increase in laser power, the peaks of *A*_g¹ and *A*_g³ modes also exhibited significant redshifts because of the laser heating effect, as shown in Figure 2d. In order to intuitively show the shift in peak position with temperature and power, we fit the peaks of *A*_g¹ and *A*_g³ modes in Figure 3. The two peaks exhibited the same trend. The *A*_g³ peak was more apparent than the *A*_g¹ peak, and the former's redshift was more remarkable. This result indicates that *A*_g³ mode is more sensitive to temperature, so we selected the *A*_g³ peak shift on a microscale as the temperature meter.

The evolution of the peak frequency, ω , as a function of the temperature was linearly fit by the equation $\omega = \omega_0 + \chi T$, where ω_0 intercepted with the temperature at 0 K and $\chi = \delta\omega/\delta T$ was the first order of the temperature coefficient. Figure 3a,b shows the linear fitting results of the *A*_g³ mode with respect to temperature in the *x*- and *y*-directions. The derived slopes related to temperature are $\chi_x = -0.00867$ and $\chi_y = -0.00881$ cm^{−1} K^{−1}; they exhibited a lattice orientation dependence. The *A*_g³ peak shift was also measured as a function of laser power for the suspended PdSe₂. When the laser power was increased, the noticeable Raman peak shift due to phonon softening caused by the suspended film's temperature increased. Under a different laser power, the frequency fitting of the *A*_g³ mode, as shown in Figure 3d,e, derived slopes ($\delta\omega/\delta P$) in the *x*- and *y*-directions equal to -0.00301 and -0.00264 cm^{−1} (μW)^{−1}, respectively. Obtaining the relationship between Raman peak

shift and the calculated temperature, the average temperature (inside the laser spot) caused by the incident laser is expressed in the formula as [43]:

$$T_m = \frac{\int_0^R T(r)q(r)rdr}{\int_0^R q(r)rdr} \quad (1)$$

where R is the radius of the hole, and r is the value of position from the center of the hole. Furthermore, we needed to consider the interfacial heat transfer and boundary conditions (see the Supplementary Material Note S2 for details). Figure 4a shows the relation between the average temperature and the thermal conductivity of the suspended films. In addition, we further obtained the expression curve of $\delta T_m / \delta P$ and the thermal conductivity, as shown in Figure 4b, which was easily obtained by our experiment.

From the above discussion, the thermal conductivity of 7.2 nm thickness PdSe₂ along the x - and y -directions were calculated to be 28.45 and 25.35 W m^{−1} K^{−1}, respectively. The extracted thickness-dependent thermal conductivity is shown in Figure 4c, indicating the existence of robust anisotropy in the few-layered PdSe₂, with an anisotropy ratio as high as 1.42 (for the calculation of the error bar, see the Supplementary Material Note S3). Such thickness-dependent anisotropic thermal conductivity has been observed in few-layered Te and BP [29,30]. By increasing the thickness of PdSe₂, the anisotropy of thermal conductivity decreased gradually in the in-plane, as shown in Figure 4d. (The thickness was determined by AFM, as shown in Figure S3). The thermal conductivity ratio (κ_x / κ_y) decreased from 1.42 to 1.08 because of the thermal conductivity in the x -direction but increased faster than the y -direction with increasing thickness. This size effect resulted from strong surface scattering of longer mean-free-path phonons [30]. The relatively thinner PdSe₂ had a lower group velocity and a longer phonon lifetime and was more likely to be affected by surface defects. The anisotropic thermal conductivity was mainly attributed to phonon scattering along the x -direction more than the y -direction, and the anisotropy of phonon scattering decreases with an increase in thickness [22]. The strong size effects on thermal and electric transport due to surface scattering were also observed in Bi₂Te₃ thermoelectric material [44]. In particular, as for the heat diffusion in the direction of the z -axis, the strong interlayer action of PdSe₂ may affect the experimental measurement, which requires further investigation. To get an intuitive understanding of the in-plane anisotropic thermal conductivity in PdSe₂, Table 1 summarizes the thermal conductivity of anisotropic 2D materials studied in recent years. Based on our work, the anisotropic thermal conductivity ratio of PdSe₂ was relatively large among the reported 2D materials. In contrast to previous theoretical reports [22], our experimental data are slightly higher than theoretical calculations but still on the same order of magnitude. The possible reason is the uncertainty of interfacial heat transfer between the material and the substrate [45]. However, for low-thermal-conductivity materials, most of the laser heat caused by a small speckle is concentrated in the hole, which has a minimal effect on the results.

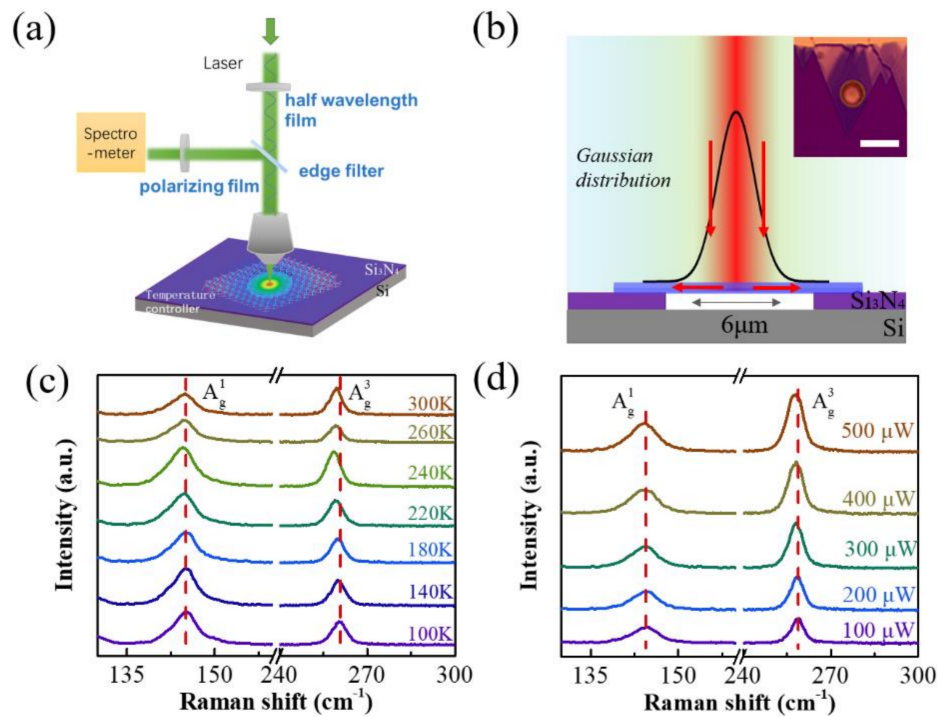


Figure 2. (a) Schematic diagram of the experimental setup for the thermal conductivity measurements. (b) Schematic of the suspended PdSe₂ on a hole 6 μm in diameter. The bar in the inset is 10 μm . (c,d) Temperature-dependent and incident-laser-power-dependent Raman spectra of the 7.2 nm-thick suspended PdSe₂ with incident laser polarization fixed along the x - and y -directions.

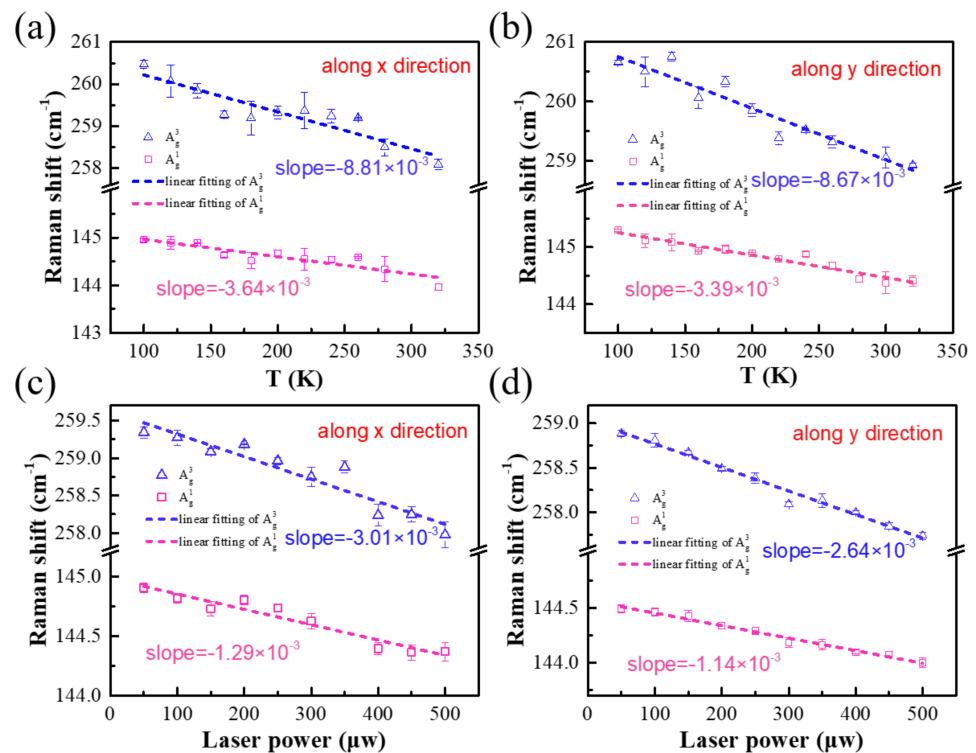


Figure 3. (a,b) were the A_g^1 and A_g^3 peak frequencies as a function of temperature along x - and y -directions, respectively. (c,d) were the A_g^1 peak frequencies as a function of laser power along the x - and y -directions, respectively.

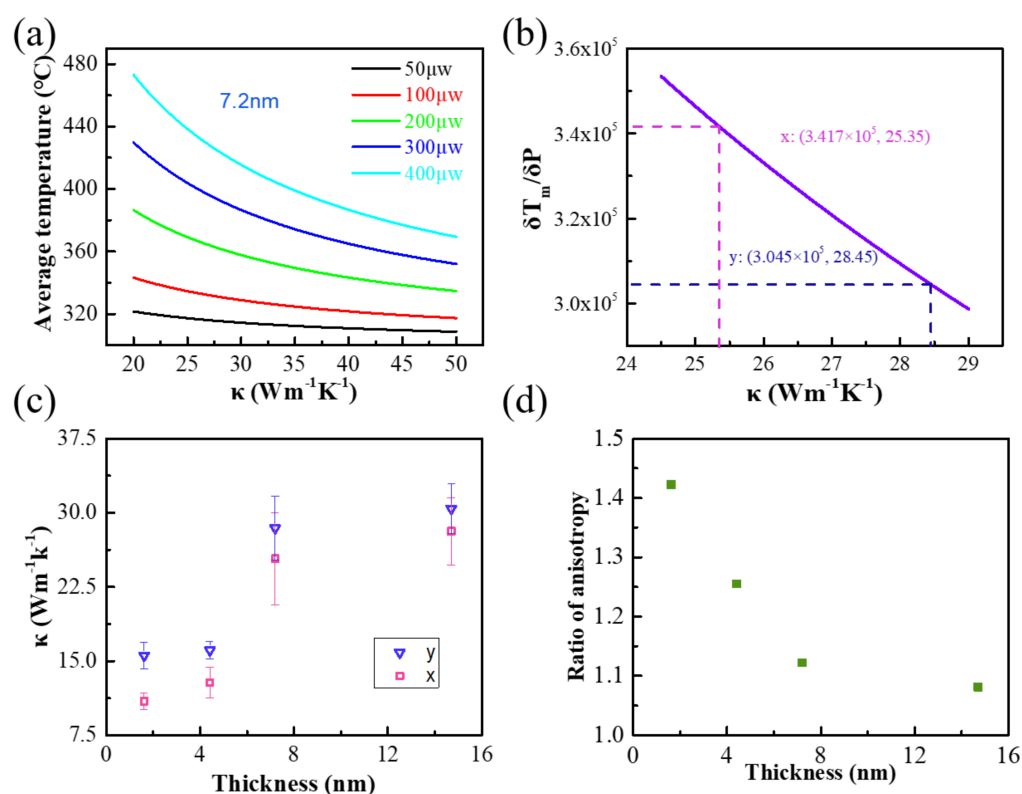


Figure 4. (a) The average temperature versus the thermal conductivity of the suspended, 7.2 nm-thick PdSe₂ nanosheet at different laser powers. (b) The calculated curve of $\delta T_m / \delta P$ as a function of the thermal conductivity. The thermal conductivity along the x- and y-directions were extracted by experimental measure. (c) The extracted in-plane thermal conductivity of different thicknesses. (d) The anisotropic ratio of thermal conductivity versus the thickness of PdSe₂.

Table 1. Thermal conductivities of anisotropic 2D materials compared.

Material	Fabrication	Thickness (nm)	Method	In-Plane κ ($\text{W m}^{-1} \text{K}^{-1}$)		Ratio	Resource
Td-WTe ₂	Exfoliation	11.2	Micro-Raman thermometry (MRT)	0.639	0.743	1.16	Ref. [26]
TiS ₃	Exfoliation	100	Thermal bridge	2.84	5.78	2.04	Ref. [46]
Te	phase syntheses	100	MRT	1.7	2.15	1.26	Ref. [30]
BP	Exfoliation	9.5	MRT	~10	~20	2.00	Ref. [29]
ReS ₂	Exfoliation	150	Time-domain thermoreflectance (TDTR)	50	70	1.40	Ref. [47]
PdSe ₂	Exfoliation	1.62	MRT	10.95	15.58	1.42	This study

4. Conclusions

To conclude, we investigated the anisotropic in-plane thermal conductivity of the suspended 2D PdSe₂ through Raman spectroscopy. The anisotropic thermal conductivity in low-symmetry pentagonal 2D PdSe₂ was first demonstrated in our experiment. We engaged linear polarization-dependent Raman spectroscopy and absorption spectrum to determine the crystal orientation (x- and y-directions) of PdSe₂ flakes due to the strong direction dependence of the anisotropic structure. The prominent anisotropy ratio of the thermal

conductivity of PdSe₂ flakes measured by MRT was found to be 1.42. This result provides a valuable reference for anisotropic thermoelectric applications. Our study may play a ground-breaking position regarding the anisotropic in-plane thermal conductivity of PdSe₂, which will greatly facilitate applications in energy conversion and in electronic devices.

Supplementary Materials: The following are available online at <https://www.mdpi.com/article/10.3390/su13084155/s1>. Figure S1: Typical Raman spectra of PdSe₂, Figure S2: Polarized light absorption spectrum, Figure S3: Optical imaging and AFM height profiles of suspended few-layered PdSe₂, Note S1: Raman tensors fitting, Note S2: Determination of the average temperature profile through the boundary conditions, Note S3: The error bar of thermal conductance.

Author Contributions: Conceptualization, L.C. and L.L.; methodology, L.C., W.Z. and L.L.; data curation, L.C.; writing—original draft preparation, L.C., J.C., C.T., S.Y., G.L., Y.Z., P.G., and L.L.; writing—review and editing, L.C., W.Z., H.Z., J.C., C.T., S.Y., G.L., Y.Z., P.G., and L.L.; project administration, L.L.; funding acquisition, L.L. All authors have read and agreed to the published version of the manuscript.

Funding: This research was funded by the National Natural Science Foundation of China (Grant No. 51902001, 11904154), the Recruitment Program for Leading Talent Team of Anhui Province (2019-16), the Anhui Provincial Natural Science Foundation (1908085QE17), the Anhui Province Natural Science Foundation (No. 1908085MF222), and the Foundation of the State Key Laboratory of Pulsed Power Laser Technology (No. SKL2019ZR04).

Institutional Review Board Statement: Not applicable.

Informed Consent Statement: Not applicable.

Data Availability Statement: Not applicable.

Conflicts of Interest: The authors declare no conflict of interest.

References

- Novoselov, K.S.; Geim, A.K.; Morozov, S.V.; Jiang, D.; Zhang, Y.; Dubonos, S.V.; Grigorieva, I.V.; Firsov, A.A. Electric Field Effect in Atomically Thin Carbon Films. *Science* **2004**, *306*, 666–669. [\[CrossRef\]](#)
- Wang, Q.H.; Kalantar-Zadeh, K.; Kis, A.; Coleman, J.N.; Strano, M.S. Electronics and optoelectronics of two-dimensional transition metal dichalcogenides. *Nat. Nanotechnol.* **2012**, *7*, 699–712. [\[CrossRef\]](#)
- Li, L.; Han, W.; Pi, L.; Niu, P.; Han, J.; Wang, C.; Su, B.; Li, H.; Xiong, J.; Bando, Y.; et al. Emerging in—Plane anisotropic two—Dimensional materials. *InfoMat* **2019**, *1*, 54–73. [\[CrossRef\]](#)
- Ma, W.; Shabbir, B.; Ou, Q.; Dong, Y.; Chen, H.; Li, P.; Zhang, X.; Lu, Y.; Bao, Q. Anisotropic polaritons in van der Waals materials. *InfoMat* **2020**, *2*, 777–790. [\[CrossRef\]](#)
- Ciarrocchi, A.; Avsar, A.; Ovchinnikov, D.; Kis, A. Thickness-modulated metal-to-semiconductor transformation in a transition metal dichalcogenide. *Nat. Commun.* **2018**, *9*, 919. [\[CrossRef\]](#) [\[PubMed\]](#)
- Wang, Y.; Li, L.; Yao, W.; Song, S.; Sun, J.T.; Pan, J.; Ren, X.; Li, C.; Okunishi, E.; Wang, Y.Q.; et al. Monolayer PtSe₂, a New Semiconducting Transition-Metal-Dichalcogenide, Epitaxially Grown by Direct Selenization of Pt. *Nano Lett.* **2015**, *15*, 4013–4018. [\[CrossRef\]](#)
- Oyedele, A.D.; Yang, S.; Liang, L.; Puzos, A.A.; Wang, K.; Zhang, J.; Yu, P.; Pudasaini, P.R.; Ghosh, A.W.; Liu, Z.; et al. PdSe₂: Pentagonal Two-Dimensional Layers with High Air Stability for Electronics. *J. Am. Chem. Soc.* **2017**, *139*, 14090–14097. [\[CrossRef\]](#) [\[PubMed\]](#)
- Liang, Q.; Wang, Q.; Zhang, Q.; Wei, J.; Lim, S.X.; Zhu, R.; Hu, J.; Wei, W.; Lee, C.; Sow, C.; et al. High-Performance, Room Temperature, Ultra-Broadband Photodetectors Based on Air-Stable PdSe₂. *Adv. Mater.* **2019**, *31*, 1807609. [\[CrossRef\]](#)
- Cheng, P.K.; Tang, C.Y.; Ahmed, S.; Qiao, J.; Zeng, L.H.; Tsang, Y.H. Utilization of group 10 2D TMDs-PdSe₂ as a nonlinear optical material for obtaining switchable laser pulse generation modes. *Nanotechnology* **2021**, *32*, 055201. [\[CrossRef\]](#)
- Di Bartolomeo, A.; Pelella, A.; Liu, X.; Miao, F.; Passacantando, M.; Giubileo, F.; Grillo, A.; Iemmo, L.; Urban, F.; Liang, S.J. Pressure—Tunable Ambipolar Conduction and Hysteresis in Thin Palladium Diselenide Field Effect Transistors. *Adv. Funct. Mater.* **2019**, *29*, 1902483. [\[CrossRef\]](#)
- Li, L.; Wang, W.; Chai, Y.; Li, H.; Tian, M.; Zhai, T. Few-Layered PtS₂ Phototransistor on h-BN with High Gain. *Adv. Funct. Mater.* **2017**, *27*, 1701011. [\[CrossRef\]](#)
- Liu, G.; Zeng, Q.; Zhu, P.; Quhe, R.; Lu, P. Negative Poisson's ratio in monolayer PdSe₂. *Comput. Mater. Sci.* **2019**, *160*, 309–314. [\[CrossRef\]](#)
- Lei, W.; Cai, B.; Zhou, H.; Heymann, G.; Tang, X.; Zhang, S.; Ming, X. Ferroelastic lattice rotation and band-gap engineering in quasi 2D layered-structure PdSe₂ under uniaxial stress. *Nanoscale* **2019**, *11*, 12317–12325. [\[CrossRef\]](#)

14. Hellgren, N.; Berlind, T.; Gueorguiev, G.K.; Johansson, M.P.; Stafström, S.; Hultman, L. Fullerene-like BCN thin films: A computational and experimental study. *Mater. Sci. Eng. B* **2004**, *113*, 242–247. [\[CrossRef\]](#)
15. Goyenola, C.; Stafström, S.; Hultman, L.; Gueorguiev, A.G.K. Structural Patterns Arising during Synthetic Growth of Fullerene-Like Sulfocarbide. *J. Phys. Chem. C* **2012**, *116*, 21124–21131. [\[CrossRef\]](#)
16. Zhang, G.; Amani, M.; Chaturvedi, A.; Tan, C.; Bullock, J.; Song, X.; Kim, H.; Lien, D.-H.; Scott, M.C.; Zhang, H.; et al. Optical and electrical properties of two-dimensional palladium diselenide. *Appl. Phys. Lett.* **2019**, *114*, 253102. [\[CrossRef\]](#)
17. Jiang, S.; Xie, C.; Gu, Y.; Zhang, Q.; Wu, X.; Sun, Y.; Li, W.; Shi, Y.; Zhao, L.; Pan, S.; et al. Anisotropic Growth and Scanning Tunneling Microscopy Identification of Ultrathin Even-Layered PdSe₂ Ribbons. *Small* **2019**, *15*, 1902789. [\[CrossRef\]](#) [\[PubMed\]](#)
18. Yu, J.; Kuang, X.; Gao, Y.; Wang, Y.; Chen, K.; Ding, Z.; Liu, J.; Cong, C.; He, J.; Liu, Z.; et al. Direct Observation of the Linear Dichroism Transition in Two-Dimensional Palladium Diselenide. *Nano Lett.* **2020**, *20*, 1172–1182. [\[CrossRef\]](#)
19. Zhong, J.; Yu, J.; Cao, L.; Zeng, C.; Ding, J.; Cong, C.; Liu, Z.; Liu, Y. High-performance polarization-sensitive photodetector based on a few-layered PdSe₂ nanosheet. *Nano Res.* **2020**, *13*, 1780–1786. [\[CrossRef\]](#)
20. Xu, W.; Jiang, J.; Ma, H.; Zhang, Z.; Li, J.; Zhao, B.; Wu, R.; Yang, X.; Zhang, H.; Li, B.; et al. Vapor phase growth of two-dimensional PdSe₂ nanosheets for high-photoresponsivity near-infrared photodetectors. *Nano Res.* **2020**, *13*, 2091–2097. [\[CrossRef\]](#)
21. Sun, J.; Shi, H.; Siegrist, T.; Singh, D.J. Electronic, transport, and optical properties of bulk and mono-layer PdSe₂. *Appl. Phys. Lett.* **2015**, *107*, 153902. [\[CrossRef\]](#)
22. Lan, Y.-S.; Chen, X.-R.; Hu, C.-E.; Cheng, Y.; Chen, Q.-F. Penta-PdX₂ (X = S, Se, Te) monolayers: Promising anisotropic thermoelectric materials. *J. Mater. Chem. A* **2019**, *7*, 11134–11142. [\[CrossRef\]](#)
23. Zhao, Y.; Yu, P.; Zhang, G.; Sun, M.; Chi, D.; Hippalgaonkar, K.; Thong, J.T.L.; Wu, J. Low—Symmetry PdSe₂ for High Performance Thermoelectric Applications. *Adv. Funct. Mater.* **2020**, *30*, 2004896. [\[CrossRef\]](#)
24. Qin, D.; Yan, P.; Ding, G.; Ge, X.; Song, H.; Gao, G. Monolayer PdSe₂: A promising two-dimensional thermoelectric material. *Sci. Rep.* **2018**, *8*, 2764. [\[CrossRef\]](#) [\[PubMed\]](#)
25. Sun, M.; Chou, J.P.; Shi, L.; Gao, J.; Hu, A.; Tang, W.; Zhang, G. Few-Layer PdSe₂ Sheets: Promising Thermoelectric Materials Driven by High Valley Convergence. *ACS Omega* **2018**, *3*, 5971–5979. [\[CrossRef\]](#)
26. Chen, Y.; Peng, B.; Cong, C.; Shang, J.; Wu, L.; Yang, W.; Zhou, J.; Yu, P.; Zhang, H.; Wang, Y.; et al. In-Plane Anisotropic Thermal Conductivity of Few-Layered Transition Metal Dichalcogenide Td-WTe₂. *Adv. Mater.* **2019**, *31*, 1804979. [\[CrossRef\]](#)
27. Wang, T.; Han, M.; Wang, R.; Yuan, P.; Xu, S.; Wang, X. Characterization of anisotropic thermal conductivity of suspended nm-thick black phosphorus with frequency-resolved Raman spectroscopy. *J. Appl. Phys.* **2018**, *123*, 145104. [\[CrossRef\]](#)
28. Soini, M.; Zardo, I.; Uccelli, E.; Funk, S.; Koblmüller, G.; Fontcuberta i Morral, A.; Abstreiter, G. Thermal conductivity of GaAs nanowires studied by micro-Raman spectroscopy combined with laser heating. *Appl. Phys. Lett.* **2010**, *97*, 263107. [\[CrossRef\]](#)
29. Luo, Z.; Maassen, J.; Deng, Y.; Du, Y.; Garrelts, R.P.; Lundstrom, M.S.; Ye, P.D.; Xu, X. Anisotropic in-plane thermal conductivity observed in few-layer black phosphorus. *Nat. Commun.* **2015**, *6*, 8572. [\[CrossRef\]](#)
30. Huang, S.; Segovia, M.; Yang, X.; Koh, Y.R.; Wang, Y.; Ye, P.D.; Wu, W.; Shakouri, A.; Ruan, X.; Xu, X. Anisotropic thermal conductivity in 2D tellurium. *2D Mater.* **2019**, *7*, 015008. [\[CrossRef\]](#)
31. Puzos, A.A.; Oyedele, A.D.; Xiao, K.; Haglund, A.V.; Sumpter, B.G.; Mandrus, D.; Geohegan, D.B.; Liang, L. Anomalous interlayer vibrations in strongly coupled layered PdSe₂. *2D Mater.* **2018**, *5*, 035016. [\[CrossRef\]](#)
32. Zeng, L.-H.; Wu, D.; Lin, S.-H.; Xie, C.; Yuan, H.-Y.; Lu, W.; Lau, S.P.; Chai, Y.; Luo, L.-B.; Li, Z.-J.; et al. Controlled Synthesis of 2D Palladium Diselenide for Sensitive Photodetector Applications. *Adv. Funct. Mater.* **2019**, *29*, 1806878. [\[CrossRef\]](#)
33. Grønvold, F.; Røst, E. The crystal structure of PdSe₂ and PdS₂. *Acta Crystallogr.* **1957**, *10*, 329–331. [\[CrossRef\]](#)
34. Zhang, S.; Zhou, J.; Wang, Q.; Chen, Q.; Kawazoe, Y.; Jena, P. Penta-graphene: A new carbon allotrope. *Proc. Natl. Acad. Sci. USA* **2015**, *112*, 2372–2377. [\[CrossRef\]](#) [\[PubMed\]](#)
35. Li, X.; Meng, S.; Sun, J.-T. Emergence of d-orbital magnetic Dirac fermions in a MoS₂ monolayer with squared pentagon structure. *Phys. Rev. B* **2020**, *101*, 144409. [\[CrossRef\]](#)
36. Wu, P. The Study for Two-dimensional PtX₂ (X = S Se Te) Which Have Geometrical Structures Fully Composed of Pentagons. *IOP Conf. Ser. Mater. Sci. Eng.* **2019**, *631*, 042010. [\[CrossRef\]](#)
37. Yang, H.; Li, Y.; Yang, Z.; Shi, X.; Lin, Z.; Guo, R.; Xu, L.; Qu, H.; Zhang, S. First-principles calculations of the electronic properties of two-dimensional pentagonal structure XS₂ (X = Ni, Pd, Pt). *Vacuum* **2020**, *174*, 109176. [\[CrossRef\]](#)
38. Long, M.; Wang, Y.; Wang, P.; Zhou, X.; Xia, H.; Luo, C.; Huang, S.; Zhang, G.; Yan, H.; Fan, Z.; et al. Palladium Diselenide Long-Wavelength Infrared Photodetector with High Sensitivity and Stability. *ACS Nano* **2019**, *13*, 2511–2519. [\[CrossRef\]](#)
39. Wang, J.; Zhou, Y.J.; Xiang, D.; Ng, S.J.; Watanabe, K.; Taniguchi, T.; Eda, G. Polarized Light-Emitting Diodes Based on Anisotropic Excitons in Few-Layer ReS₂. *Adv. Mater.* **2020**, *32*, 2001890. [\[CrossRef\]](#)
40. Li, L.; Wang, W.; Gong, P.; Zhu, X.; Deng, B.; Shi, X.; Gao, G.; Li, H.; Zhai, T. 2D GeP: An Unexploited Low-Symmetry Semiconductor with Strong In-Plane Anisotropy. *Adv. Mater.* **2018**, *30*, 1706771. [\[CrossRef\]](#)
41. Sahoo, S.; Gaur, A.P.S.; Ahmadi, M.; Guinel, M.J.F.; Katiyar, R.S. Temperature-Dependent Raman Studies and Thermal Conductivity of Few-Layer MoS₂. *J. Phys. Chem. C* **2013**, *117*, 9042–9047. [\[CrossRef\]](#)
42. Araujo, F.D.V.; Oliveira, V.V.; Gadelha, A.C.; Carvalho, T.C.V.; Fernandes, T.F.D.; Silva, F.W.N.; Longuinhos, R.; Ribeiro-Soares, J.; Jorio, A.; Souza Filho, A.G.; et al. Temperature-dependent phonon dynamics and anharmonicity of suspended and supported few-layer gallium sulfide. *Nanotechnology* **2020**, *31*, 495702. [\[CrossRef\]](#) [\[PubMed\]](#)

-
43. Cai, W.; Moore, A.L.; Zhu, Y.; Li, X.; Chen, S.; Shi, L.; Ruoff, R.S. Thermal transport in suspended and supported monolayer graphene grown by chemical vapor deposition. *Nano Lett.* **2010**, *10*, 1645–1651. [[CrossRef](#)] [[PubMed](#)]
 44. Pettes, M.T.; Maassen, J.; Jo, I.; Lundstrom, M.S.; Shi, L. Effects of surface band bending and scattering on thermoelectric transport in suspended bismuth telluride nanoplates. *Nano Lett.* **2013**, *13*, 5316–5322. [[CrossRef](#)]
 45. Peimyoo, N.; Shang, J.; Yang, W.; Wang, Y.; Cong, C.; Yu, T. Thermal conductivity determination of suspended mono- and bilayer WS₂ by Raman spectroscopy. *Nano Res.* **2014**, *8*, 1210–1221. [[CrossRef](#)]
 46. Liu, H.; Yu, X.; Wu, K.; Gao, Y.; Tongay, S.; Javey, A.; Chen, L.; Hong, J.; Wu, J. Extreme In-Plane Thermal Conductivity Anisotropy in Titanium Trisulfide Caused by Heat-Carrying Optical Phonons. *Nano Lett.* **2020**, *20*, 5221–5227. [[CrossRef](#)]
 47. Jang, H.; Ryder, C.R.; Wood, J.D.; Hersam, M.C.; Cahill, D.G. 3D Anisotropic Thermal Conductivity of Exfoliated Rhenium Disulfide. *Adv. Mater.* **2017**, *29*, 1700650. [[CrossRef](#)]